Pergamon

PII: S0191–8141(98)00023–6

Journal of Structural Geology, Vol. 20, No. 7, pp. 865 to 881, 1998

0191-8141/98 $19.00 + 0.00

Laboratory characterization of hydromechanical properties of a seismogenic normal fault system

BERNARD SERONT and TENG-FONG WONG

Department of Geosciences, State University of New York at Stony Brook, Stony Brook, NY 11794, U.S.A.

JONATHAN S. CAINE, CRAIG B. FORSTER* and RONALD L. BRUHN

Department of Geology and Geophysics, University of Utah, U.S.A.

and

J. T. FREDRICH

Geomechanics Department, Sandia National Laboratories, Albuquerque, New Mexico, U.S.A.

(*Received* 18 *September* 1996; *accepted in revised form* 29 *January* 1998)

Abstract—The Stillwater seismogenic normal fault in Dixie Valley, Nevada has been historically active and is located in an area of high heat flow and hydrothermal activity. Three primary structural elements are identified in the fault zone: a relatively wide fault core (with breccia pods embedded in cataclasites), a damage zone (with arrays of mesoscopic fractures), and protolith. Hydromechanical properties of representative core samples were characterized in the laboratory, and microstructural analyses were conducted using optical and scanning electron microscopy. When deformed in conventional triaxial compression, dilatancy and brittle fracture were observed in each sample. Samples from the core of the fault were relatively weak, with strengths similar to that of unconsolidated fault gouge, whereas granodiorite samples from the protolith were as weak as the core and damage zone samples were stronger. Permeability is dependent on effective pressure, porosity and connectivity of the pore space, with values ranging over four orders of magnitude among the core samples. The lowest permeability of 3×10^{-20} m^2 was measured in a fault core sample with a microstructure indicative of implosion brecciation. In conjunction with field measurements, the laboratory data suggest that fluid flow and changes in fluid storage are concentrated in the damage zone, with permeability several orders of magnitude higher than the protolith and fault core. Permeability contrast (one order of magnitude) at the core sample scale exists between the cataclasite and implosion breccia in the fault core. Because of dilatancy and poor drainage in the breccia pods, anomalously low pore pressures may develop in localized clusters due to dilatancy hardening during the preseismic period. These clusters of low pore pressure can act similarly to fault jogs, locally inhibiting fault rupture and inducing brecciation when the delayed failure finally occurs by catastrophic implosion.

INTRODUCTION

A growing body of evidence suggests that fluids exert significant mechanical and chemical influences on faulting processes. Conceptual models incorporating spatial and temporal variations in the hydromechanical behavior have been proposed to analyze the evolution of stress and failure in a seismogenic system during the earthquake cycle (see review by Hickman *et al.*, 1995).

The earthquake cycle is interpreted to be a continual competition between processes that cause the creation and destruction of fluid pathways (Byerlee, 1993). The resulting temporal changes in permeability may cause intermittent fluid flow along localized pathways (Sibson, 1994). Furthermore, the fault zone architecture and permeability structure may control the coupling of earthquake rupture and fluid flow as indicated by their hydrologic (Sibson, 1994) and structural (Sibson, 1986a) signatures.

The overall objective of this study is to characterize the heterogeneity in hydromechanical attributes of an active normal fault zone using field and laboratory studies. Caine was responsible for the detailed field mapping; sampling; the initial hand sample and microscopic descriptions; and for developing the original structural, hydrogeologic, and mechanical conceptual models (Caine *et al.*, 1996). Permeability and mechanical deformation measurements on hand samples selected from each part of the fault zone were conducted in the Stony Brook laboratory, where additional detailed microscopic observations were performed to characterize lithology, pore geometry, cementation, damage structure, and failure mode. In this paper, the laboratory and microstructural observations were synthesized and integrated into the original conceptual models to include the mechanism of dilatancy hard-

*Now at Energy & Geoscience Institute, Department of Civil and Environmental Engineering, University of Utah, U.S.A.

ening in the context of the earthquake cycle and to provide insight into fluid–rock interaction and its control on strength and permeability within the fault zone.

SEISMOTECTONIC SETTING

The Stillwater fault zone (Fig. 1) is part of a 300-km-long-belt of normal and oblique normal faults in central Nevada. This fault system lies in an area of high heat flow, late Cenozoic volcanic activity, and recent seismic activity. Historic earthquakes that generated scarps within the belt include (from north to south): the Tobin Range–Pleasant Valley (1915, $M = 7.7$), Fairview Peak–Dixie Valley (1954, $M = 6.8$), Wonder (1903), Cedar Mountains (1932), Excelsior Mountains (1934), Mammoth Lakes (1980), and Owens Valley (1872) earthquakes (Wallace and Whitney, 1984). The Tobin range event was one of the largest normal faulting earthquakes in history.

Several features motivated us to study this fault system. The Stillwater fault is very well exposed and is an active normal fault system capable of generating $M > 6$ earthquakes. The 1954 earthquake rupture along the eastern base of the Stillwater Range was 30–40 km long with a hypocenter located at a depth in excess of 12 km. Granitic to gabbroic rocks found in the footwall of the fault zone are representative of rock types commonly found in the continental crust. The rocks exposed at the 1954 fault segment contain minerals and fluid inclusions which serve as excellent indicators of the pressure and temperature conditions during fluid circulation and fluid assisted alteration within the fault zone (Parry *et al.*, 1991). At our study locality, called the 'Mirrors', earthquakes have not occurred in historic times and microseismicity is minimal (Dozer, 1986). Because the Mirrors locality is found between and is aligned with the northern (Tobin Range 1915) and southern (1954 earthquake) fault segments, which have been active during the past 12,000 years, it is considered to be within a seismic gap in the Stillwater fault zone and may be a probable site for a large earthquake in the future (Wallace and Whitney, 1984). Finally, considering the features described above, the results of our study will be directly applicable to active normal faults found elsewhere.

At the Mirrors locality, the rocks that constitute the basement of the fault form the Stillwater Range. They are mainly Upper Jurassic to Mesozoic gabbroic and dioritic rocks and early, variably metamorphosed, Cretaceous granodiorites (Page, 1965). These units are overlain by a Tertiary volcanic sequence. Dixie Valley itself is a graben filled with late Pleistocene and Quaternary alluvial sediments that overlie the Tertiary volcanic rocks that correspond to those found in the Stillwater Range. Relative displacement of the volcanic sequence between the Stillwater Range and the graben

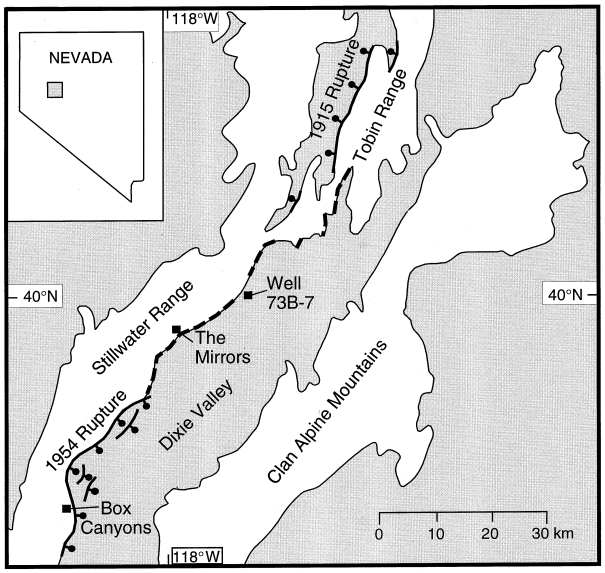

Fig. 1. Regional map of the Stillwater fault zone, Dixie Valley, Nevada, U.S.A. showing the study localities. Location of the well (73B-7) studied by Hickman *et al.* (1995) is also indicated. Heavy lines with ball and stick marks denote the downthrown fault block. The heavy dashed lines show fault segments thought to be seismic gaps. Highlands are shaded and lowlands are not. Modified from Power and Tullis (1989).

floor suggests that total displacement on the fault is approximately 3–6 km, generally increasing southwards (Parry *et al.*, 1991; Power and Tullis, 1989).

Hydrothermal alteration is present along the entire fault zone, as described in detail by Parry *et al.* (1991) along the 1954 rupture segment. In the samples we studied, hydrothermal activity is marked by the presence

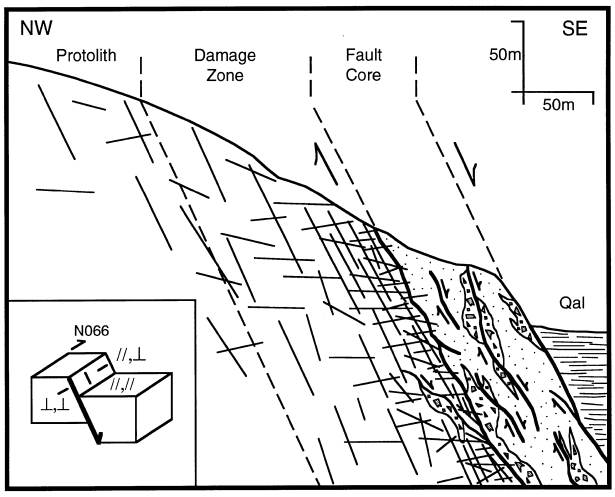

Fig. 2. Schematic cross section through the Stillwater normal fault zone at the Mirrors Locality. The fault core is composed of cataclasites (stippled pattern) and embedded breccia pods (breccia pattern which is not to scale). The insert shows the notation used for the orientation of different core samples (small lines) collected in each component of the fault zone: //,// represents the axis of a sample that is parallel to the slip direction in the fault plane, //,⊥ is parallel to the fault plane, normal to the slip direction, and ⊥,⊥ is normal to the fault plane and normal to the slip direction. The average orientation of the fault zone is 066/55SE. This figure and the corresponding conceptual model is based on original field mapping and its subsequent interpretation completed by J. S. Caine.

of the following minerals: potassium feldspar, biotite, epidote, chlorite, smectite, kaolinite, chalcedony, quartz, calcite and dolomite. Silicification of the footwall rocks is due to fluid circulation through the fault zone and is extensive (Forster *et al.*, 1997; Power and Tullis, 1989).

Hydraulic fracturing measurements in the geothermal reservoir hosted in the Stillwater fault indicate that the *in situ* stresses are consistent with W–NW extensional deformation (normal faulting). The least horizontal principal stress is in accord with frictional faulting theory for a strong fault assuming hydrostatic fluid pressure and a coefficient of friction of 0.6–1.0 (Hickman and Zoback, 1997).

A schematic cross section of the fault zone at the Mirrors locality is shown in Fig. 2. Following the structural nomenclature described by Caine *et al.* (1996), we define two basic structural components in the fault zone: a fault core and a damage zone. The undeformed rock adjacent to the fault is termed protolith (Fig. 2). The fault core is the active part of the fault where large strain is pervasive. The damage zone is more difficult to define. We identify it as the region where accumulated strain or localized slip is minimal, but brittle deformation is greater than that of the surrounding protolith. The damage zone typically includes extensive fracture and vein networks, but can also include subsidiary faults and localized zones where cataclasis has occurred. The transitional boundary between the damage zone and the protolith is marked by a decrease in fracture intensity that makes the contact difficult to precisely locate. Identifying this contact is additionally complicated because estimates of fracture intensity depend on the scale of observation.

PETROPHYSICAL CHARACTERIZATION

Two areas of the Stillwater fault system were studied in detail: the Box Canyons and the Mirrors localities. The Box Canyon locality is situated on the 1954 rupture segment (39°38′ N 118°11′ W, referenced as '1954 rupture fault segment' on Fig. 1). Total displacement across the fault is about 6 km (Parry *et al.*, 1991). The clearly visible scarp from the 1954 earthquake is located in Quaternary sediments. Although sediments cover the fault core at the scarp, several side canyons, oriented perpendicular to the fault, offer good cross sectional views through the damage zone to the protolith. The Mirrors locality is situated in footwall rocks within the Stillwater seismic gap (39°57′ N, 117°57′ W, Fig. 1). Holocene scarps found in the region are evidence of large earthquakes during the last 12,000 years (Wallace and Whitney, 1984). The Mirrors locality is so named because it exposes large, striated and polished slip surfaces over 100 m^2 in area. This part of the fault zone provides good exposures of the fault core. Total displacement at the Mirrors locality is estimated at 3–6 km, even though the exposed slickenside surfaces were formed at depths of less than 2 km (Power and Tullis, 1989).

The fault core, damage zone and protolith samples were characterized at several different scales. Field observations provide the general structure of the fault zone and the geometry of each fault-related component (Forster *et al.*, 1997). Detailed laboratory studies of representative samples from each structural component were completed with observations made at the hand sample, optical and electron microscopic scales.

Each core sample was carefully oriented with respect to the average orientation of the fault plane and the slip direction (Fig. 2, insert). The following notations were used:

$\perp\perp$: The axis of the core is perpendicular to the fault plane and the slip direction.
$///$: The axis of the core lies on the fault plane along the slip direction.
$//\perp$: The axis of the core lies on the fault plane perpendicular to the slip direction.

In addition to the orientation designations above, each sample is named according to its structural significance using the following notation and all samples are from the Mirrors locality unless specified:

PL: protolith sample (e.g. **PL**$\perp\perp$ signifies structural position and orientation).
DZ: damage zone sample (all of these are from the Box Canyon locality).
CATA: cataclasite from the fault core.
MB: microbreccia from the fault core.
IB: implosion breccia sample from the fault core.

Modal compositions of the samples were determined by X-ray diffraction (XRD). The grain and pore sizes of the fault core samples are too small to be resolved optically. Selected fault core samples were therefore studied further using scanning electron microscopy (SEM) and microprobe analysis of ion-milled crack-sections.

Interconnected porosities were measured on each sample before and after the permeability testing. The sample was weighed dry (ω_d), vacuum saturated with distilled water, and weighed again (ω_w). The interconnected porosity of the sample is: $\phi = (\omega_w - \omega_d)/(\rho_w V)$ where ρ_w is the water density of and V the volume of the sample. The absolute uncertainty is on the order of $\pm 0.2\%$, as estimated by repeated measurements on the same sample.

The petrophysical characteristics are summarized in Table 1, and detailed descriptions are provided below.

Fault core

The fault core samples are characterized by intense grain size reduction through cataclasis, the occurrence of brecciation, and the presence of slip or slickenside surfaces. Field observations indicate that the fault core

Table 1. Petrophysical description of the tested samples

Sample	ϕ (%)	Modal analysis (wt%)	Description	Location	Grain size
PL$\parallel\perp$	5.2	Qu 11, Pl 68,	Altered granodiorite. Significant intragranular porosity, but low fracture density.	Mirrors locality, protolith.	
PL$\perp\perp$	5.6	Fk 4, Cl & Sm 9			0.5–1 mm
DZ1$\parallel\parallel$	1.2	Qu 18, Pl 35, Fk 30, Cl & Sm 5 (1)	Fresh granodiorite. Very low fracture density.	Box Canyon, damage zone.	1.5–2 mm
DZ2$\parallel\parallel$	1.6	Qu $\sim$ 20,Pl & Fk $\sim$ 60, Cl & Sm $>$15, Am & Ox $<$5 (2)	Altered granodiorite, highly fractured.	Box Canyon, ultra damaged carapace.	mm
CATA$\parallel\perp$	0.3		Fine-grain cataclasite, fracture density low. Long intergranular, only partially filled fractures.	Mirrors locality, fault core.	
CATA$\perp\perp$	0.4	Qu 61, Ka 29, Ox 5, Ca 1			$<10\ \mu$m
MB$\perp\perp$	2.8	Qu 64, Ka 21, Ca & Do 7, Ox 5	Microbreccia. Extensive fracture and vein network partially cemented with quartz.	Mirrors locality, fault core.	$<10\ \mu$m
IB$\parallel\parallel$	3.6	Qu 75, Ka 5, Am & Ox 9, Ca & Do 7	Jigsaw textured breccia, angular clasts, hydrothermal quartz kaolinite matrix.		clasts: cm–$>$ m
IB$\parallel\perp$	3.8			Mirrors locality, fault core.	matrix: μm
IB$\perp\perp$	3.3				

Qu: quartz, Pl: plagioclase, Fk: K feldspar, Cl: chlorite, Ka: Kaolinite, Sm: smectite, Ca: calcite, Do: dolomite, Ox: oxides, Am: amorphous. $\phi$is the porosity of the sample in %. The modal analysis was condensed from X-ray diffraction analysis.
(1) The actual sample tested is less altered than the one used for the X ray analysis.
(2) No X-ray analysis was available. The composition and average grain size were estimated under the optical microscope.

is predominantly made up of cataclasite and microbreccia which surrounds pods of implosion breccias. Our fault core samples (all collected at the Mirrors locality) can accordingly be separated into two groups.

The first group includes a cataclasite (**CATA**) and a microbreccia (**MB**). These samples are very similar and are characterized by a very fine-grained ($<10\ \mu$m) matrix, containing no more than 10% by volume of clast of protolithic origin. The cataclasites have a lower interconnected porosity (less than 1%), and the XRD analysis shows that these samples are completely altered and silicified, with 61% quartz, 29% kaolinite and a small amount of calcite and oxides (Table 1). In hand samples and under the optical microscope, the cataclasites show a small number of intergranular microfractures, with lengths in the 10–100 mm range, which are filled with quartz. Detailed SEM observations revealed a few elongated microcracks which are completely open, usually with apertures as small as 1 μm (Fig. 3a). Nearly all the fractures are tortuous and only partially filled, mostly with quartz (Fig. 3a), but in some places they are filled with calcite. The microbreccia sample shows features indicative of a superposed deformation event which created a pervasive network of fractures and veins filled with crushed ultrafine-grained material (Fig. 3b). The fracturing is so intense that the rock can be characterized as a breccia with the original cataclasite now forming the clasts, in a matrix of fracture filling material (about 20% by volume) (Fig. 3b). The microbreccia has composition similar to that of the cataclasite: quartz 64%, kaolinite 21%, and minor amounts of oxides and calcite. The matrix, however, is exclusively composed of quartz. The rock has an interconnected porosity of $\sim$3% due exclusively to poorly cemented parts of the fracture and vein network. Open microcracks are seldom located in the clasts.

The second category of fault core rock, sample (**IB**), is represented by implosion breccias. These rocks are composed of angular clasts of all sizes (from <10 mm to 100 mm or more) with a jigsaw texture in a very fine-grained ($<1\ \mu$m) silicified matrix. Implosion breccias can form by catastrophic failure associated with pore fluid pressure differentials in active fault zones (Sibson, 1986a). No open microcracks are discernible at the scales studied. The clasts are internally brecciated, with the larger ones containing smaller clasts of identical breccia (Fig. 3c). This feature is recurrent at all scales, including the thin section scale where subcentimeter sized clasts often show an older brecciated or cataclastic structure, indicating the occurrence of multiple brecciation events. The most interesting feature of the rock is its matrix supported fabric revealed from image analysis of the distribution of clasts vs matrix in hand samples where the matrix represents at least 54% of the rock volume. The interconnected porosity in the matrix is surprisingly high (from $\sim$3% to 4%) and primarily composed of almost equidimensional pores (μm range) which are barely discernible under the SEM (Fig. 3d). These pores are probably connected to one another by extremely thin microcracks with apertures below the resolution ($\sim$0.02 μm) of the SEM.

Damage zone and protolith

The damage zone is extensively fractured at the outcrop scale, with a gradational decrease in fracture intensity as the protolith is approached. The rock type is granodiorite, which exhibits a variable degree of hydrothermal alteration. The fracture network is mainly mesoscopic, with fracture lengths on the order of 1–10 m (Fig. 3e).

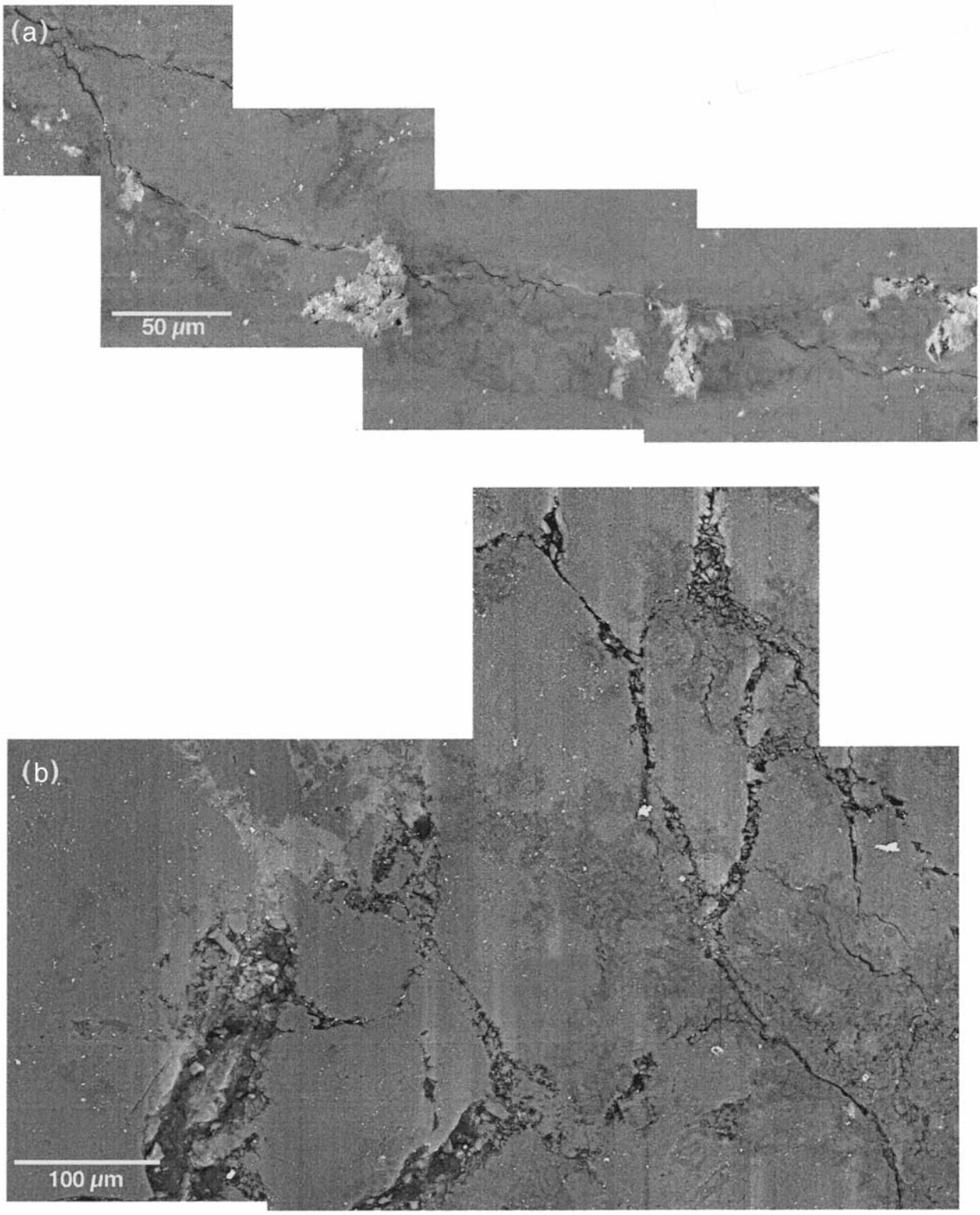

Fig. 3 (a & b).

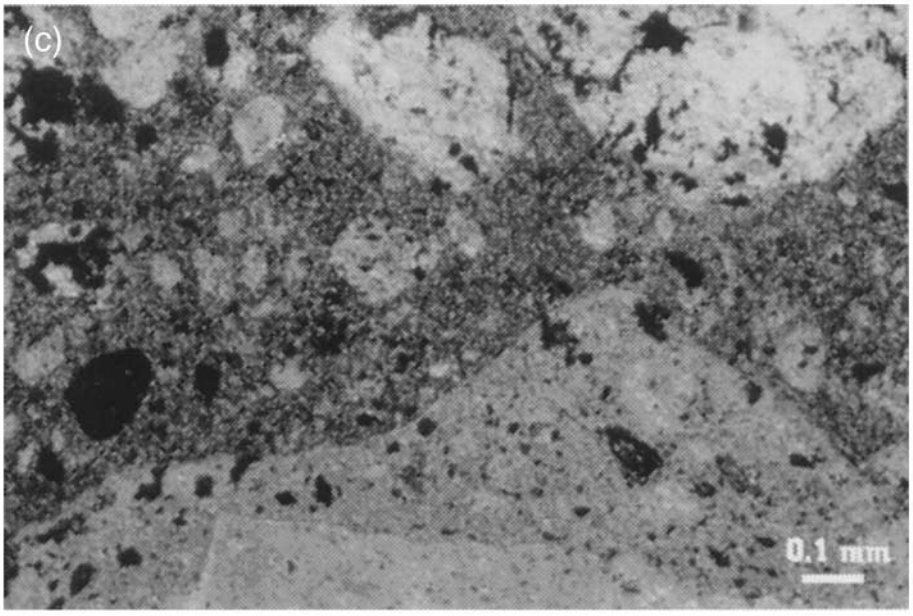

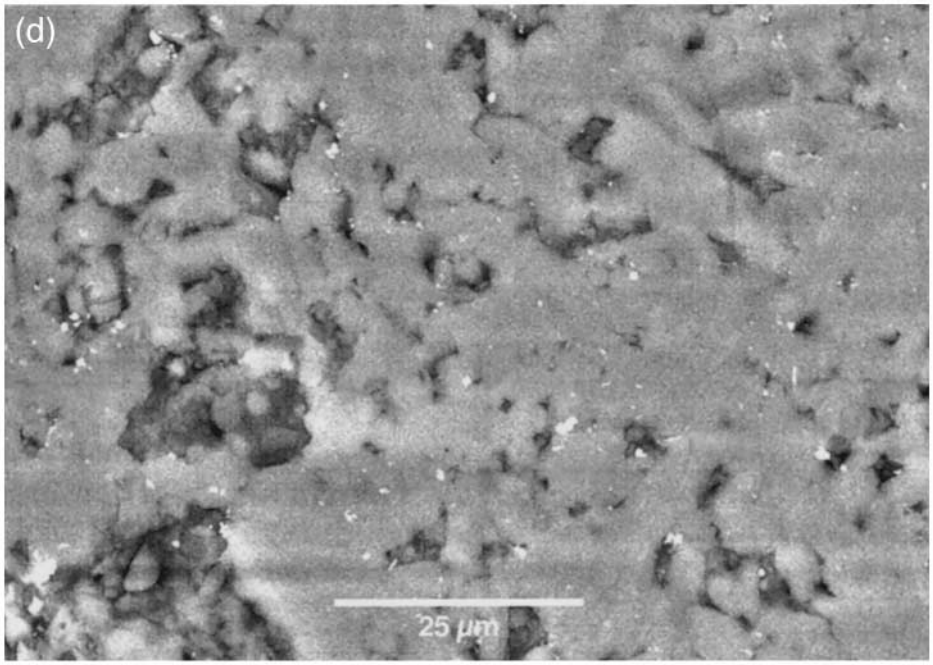

Fig. 3 (c & d).

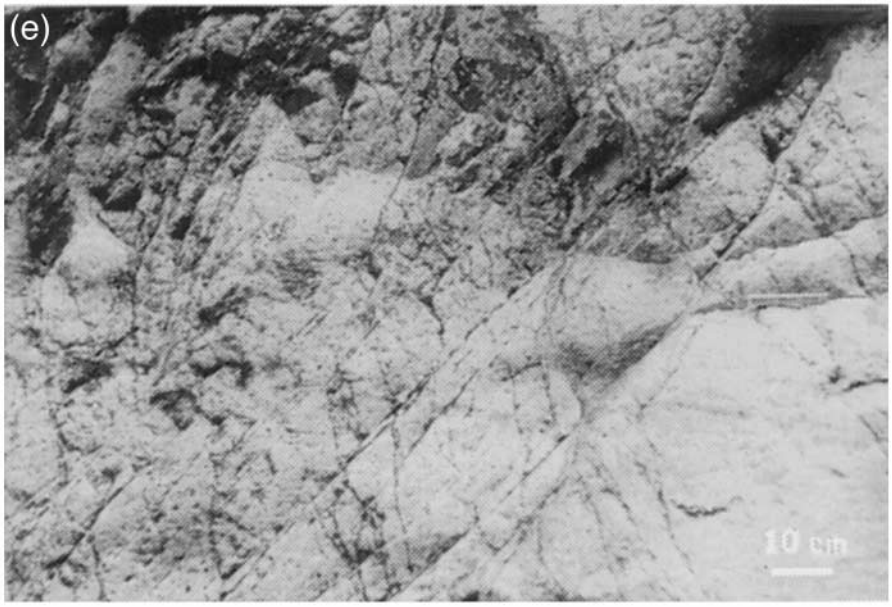

Fig. 3. (a) SEM micrograph of a cataclasite sample (**CATA**). The microcrack is typical of the structure of this rock. It is partially sealed with quartz (in white). In the background, the darker zones are kaolinite alteration, light gray material is quartz, and isolated white minerals are oxides. (b) SEM micrograph of a microbreccia (**MB**), showing the pervasive network of fractures and veins filled with ultrafine-grained crushed material. (c) Plain light optical micrograph of the implosion breccia (**IB**). The rock is made up of angular clasts variable in size with a jigsaw texture in a very fine-grained silicified matrix. The clasts themselves show internal brecciation, and the bigger ones include older clasts made of an identical type of breccia. (d) SEM micrograph of the **IB**, at high magnification, showing the pore structure of the matrix. No open microcracks are discernible at all of the scales we considered. (e) Field view of the damage zone. The fracture network is mainly mesoscopic, with fractures lengths of the order 1–10 m. The white marker is 12 cm long.

Usually the contact between the fault core and the damage zone is clearly marked by the lack of pervasive cataclasis or brecciation outside the fault core, although the damage zone does include occasional small subsidiary faults. There is no clearly marked boundary between the damage zone and the protolith, as the extent of fractures is variable along the fault. The damage zone width is estimated by mapping the fracture density across different parts of the fault is 50–100 m (Forster *et al.,* 1997).

One protolith sample (**PL**) was collected at the Mirrors locality. This rock is a fine-grained altered granodiorite. The rock contains a few long (~100 mm) widely spaced transgranular fractures. A major characteristic of the hand sample is that it contains many intergranular pores (in contrast to all the other samples), with a total interconnected porosity of from ~5% to 5.5%. The protolith at the Mirrors locality is structurally and mineralogically complex with overprints of older magmatic and tectonic events. Early Tertiary alteration and weathering of the rock are also probable. Significant alteration of the rock is manifested by the deposition of chlorite (4 wt% total) and smectite (4 wt% total) on the intergranular pore walls.

Two samples were collected from the damage zone at Box Canyon. The first sample (**DZ1**) is a granodiorite of medium grain size. The block collected has a complicated structure. Thin section examination revealed that the sample was taken on the boundary of a subsidiary shear zone. A sample was prepared for hydromechanical testing from part of the block which is not affected by the alteration related to the subsidiary shear zone, even though the petrographic analysis was performed on a more altered part of the block. The degree of alteration of the tested sample is therefore lower than that reported in Table 1, with only a few percent of chlorite–smectite alteration, and a higher plagioclase to potassium-feldspar ratio. The pore space is comprised of a small number of transgranular fractures. This sample represents a zone of relatively diffuse deformation where mesoscopic fracture sets surround pods of relatively undamaged protolith within the damage zone.

The second damage zone sample from the Box Canyon locality, **DZ2**, is a highly fractured and altered granodiorite. This sample was from a location closer to the fault core, and its microstructures are characteristic of the ultradamaged carapace. The pervasive fracture network is essentially intergranular, with fracture lengths < 10 mm. There is no preferred orientation of the fractures. Larger fractures, from the mesoscopic fracture network are also visible from place to place in the block, but care was taken to avoid such large fractures during preparation of samples for hydromechanical testing.

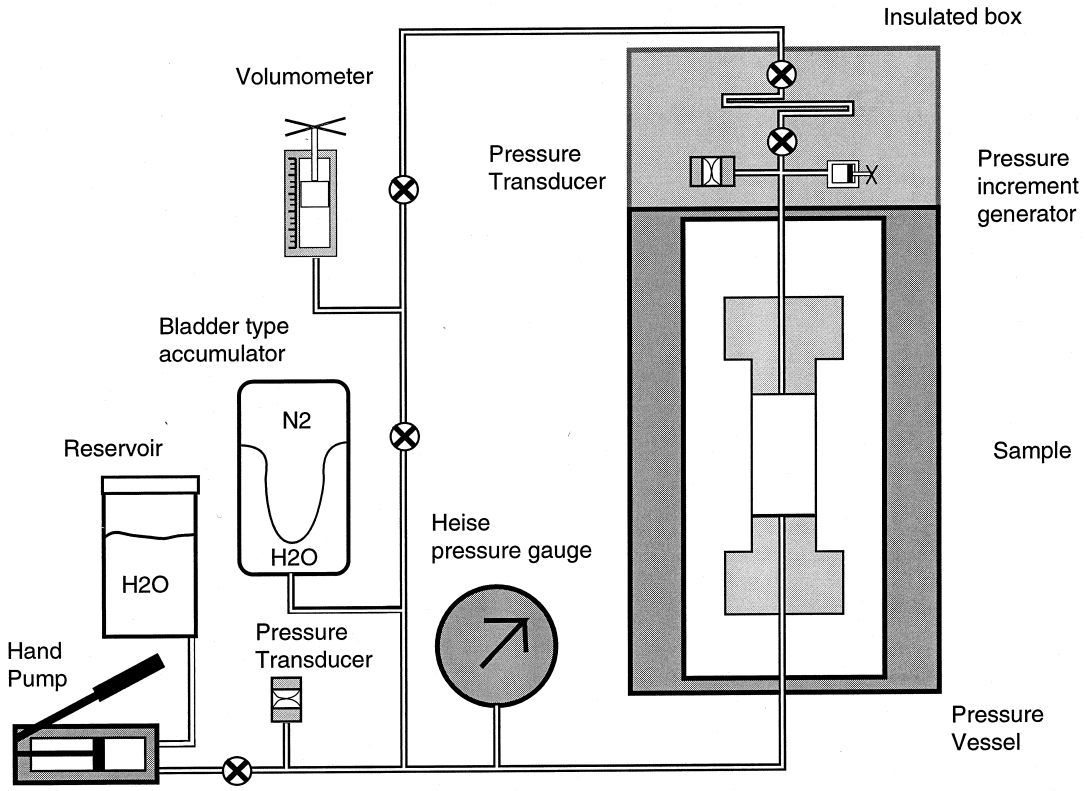

Fig. 4. Experimental setup for permeability measurements used for this study.

EXPERIMENTAL PROCEDURE

Permeability measurements

Permeability was measured as a function of effective pressure on samples saturated with distilled water. All the tests were done with the pulse transient technique introduced by Brace *et al.* (1968). An overview of our experimental setup is shown in Fig. 4. In order to achieve good accuracy in measuring permeability values as low as 10^{-20} m^2, two improvements have been made on our measurement system. First the top of the pressure vessel and the pore pressure plumbing were enclosed in an insulated box, reducing temperature variation to $<0.2^{\circ}$C. This minimizes fluctuations in the viscosity and reservoir pressure which are sensitive to temperature. Second we now have the ability to switch among three different configurations of upstream reservoir corresponding to a wide range of storage values. Since the time needed to complete a test is directly related to the value of C_u, storativity of the upstream reservoir, relatively low permeability is measurable in a reasonable time only if C_u is sufficiently small.

The measurement is conducted as follows. The pore pressure in the system is equilibrated at 10 MPa. While the downstream side of the sample is maintained at this constant pore pressure (the downstream reservoir is connected to a bladder type accumulator), a small pressure pulse ($\sim$1 MPa) is generated at the upstream end of the sample (by adjusting a valve attached to the upstream reservoir). Pressure decay in the upstream reservoir is recorded during transient fluid flow through the sample from upstream to downstream reservoirs.

If the storage of the sample is negligible compared to the storage of each reservoir the transient decay is an exponential function of time (Hsieh *et al.*, 1981; Trimmer, 1981). A semi-log plot of the pressure decay vs time is linear, with the slope given by $\alpha = (kA/\mu L)(1/C_u + 1/C_d)$ where k is the permeability, L and A are the length and cross sectional area of the sample and μ is the viscosity of the pore fluid (water) at the test temperature. C_u and C_d are the respective compressive storage of the upstream and downstream reservoirs, defined as the volume change per unit pressure change associated with each reservoir. Since the downstream reservoir is connected to the bladder type accumulator in all our experiments, C_d can be considered as infinitely large thus $1/C_d$ can be neglected in the above equation. The major source of uncertainty in the pressure decay equation is C_u, which is obtained by calibration with an impermeable aluminum sample replacing the usual rock sample. Since compressibility of the volumometer and valve packings may change somewhat, their influences on C_u are not easily quantifiable. From numerous repeated measurements we

infer that the permeability values reported here are accurate to ±10%.

Mechanical tests

Samples used for the permeability tests were subsequently deformed at room temperature in the conventional triaxial configuration. The confining pressure P_c was maintained at a constant value of 100 MPa while the pore pressure P_p was maintained at a constant value of 10 MPa by means of a volumometer connected to the pore pressure system. This allows for the measurement of the quantity of fluid draining into or out of the sample during deformation, which is a direct measure of the pore volume change. The measured volume change is referenced to the initial sample volume to infer the porosity change.

Differential stress is applied to the sample with a servo-controlled hydraulic ram at a constant displacement rate of 0.5 μm s^{-1} (corresponding to a nominal strain rate of 1×10^{-5} s^{-1}) and measured with an external load cell. This strain rate is sufficiently slow to ensure that the sample is 'drained' during the deformation. The piston displacement is measured with a displacement transducer mounted between the moving ram and the pressure vessel and corrected for the elastic deformation of the loading system (which has a stiffness of 1.9×10^8 N m^{-1}), for calculation of the axial strain (with reference to the initial length of the sample).

MECHANICAL DEFORMATION AND FAILURE MODE

The data are presented as differential stress (σ_1–σ_3) and pore volume strain vs axial strain in Fig. 5(a) (for fault core samples) and Fig. 5(b) (for damage zone and protolith samples). Positive values of axial and pore volume strains correspond to shortening and porosity reduction respectively. The onset of dilatancy is defined by the stress level C' at the transition from compaction to dilatancy, corresponding to the peak of the pore volume deformation curve. Data for Young's modulus E, C', the peak stress, and the angle θ (between the shear band and σ_1) are compiled in Table 2.

At effective pressures P_e of 90 MPa, the fault core samples attained peak stresses in the range from 430 MPa to 570 MPa (Fig. 5a). With reference to Ohnaka's (1973) compilation, these peak stress values are considered very low compared with unaltered igneous rocks. The fault core samples were weak possibly due to the relatively low cohesion and alteration mineralogy (**MB**, **CATA**, and **IB**). Dilatancy was observed to some extent in all three samples, the post-peak deformation was relatively stable, and failure developed by conjugate faulting.

The protolith samples (peak stress range: 470–540 MPa) were as weak as the fault core samples (Fig. 5a & b). For one orientation, a protolith sample was also deformed under nominally dry conditions (**PL⊥⊥dry**, Fig. 5b). It attained a peak stress comparable to that of the saturated counterpart. The dilatancy, post-peak deformation and failure mode of the protolith samples were qualitatively similar to the fault core samples. In contrast, the failure modes of the damage zone samples (**DZ1** and **DZ2**) were more 'brittle' in several respects. First, onset of dilatancy occurred relatively early in the pre-failure stage, and second, peak stresses attained are very high compared with unaltered igneous rocks (Ohnaka, 1973). Furthermore, multiple

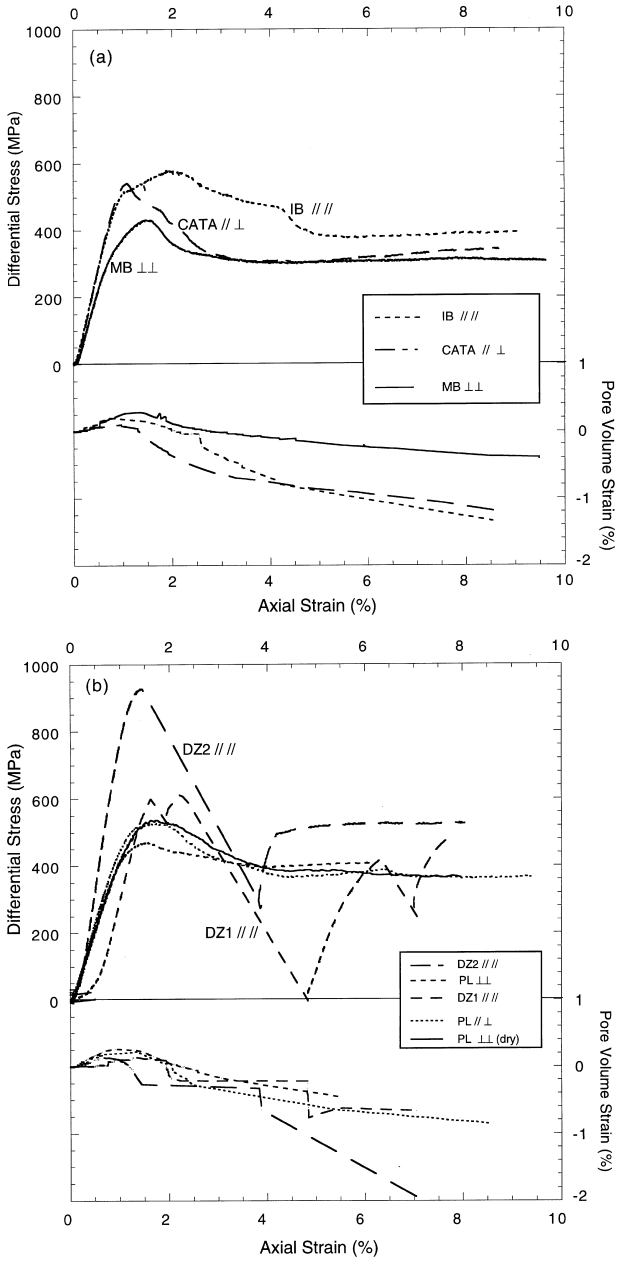

Fig. 5. Mechanical data of (a) fault core, and (b) damage zone and protolith samples.

Table 2. Hydromechanical results

Sample	E (GPa)	Peak stress (MPa)	C' (MPa)	θ	k (m^2) P_e: 15 MPa	k (m^2) P_e: 90 MPa	γ (10^{-2} MPa^{-1}) P_e:15–90 MPa [15–30, 30–90 MPa]	$\Delta\phi/\Delta P_e$ (10^{-6} MPa^{-1})	$(1/\phi_0)(\Delta\phi/\Delta P_e)$ (10^{-3} MPa^{-1}) P_e:15–90 MPa
PL //⊥	49	540	450	30°	3×10^{-16}	3×10^{-18}	6.0	43	0.9
PL⊥⊥	45	470	440	> 30°	1×10^{-16}	1×10^{-18}	6.5 [15.2–4.0]	60	1.1
DZ1///	59	610	600	35°	1×10^{-16}	1×10^{-18}	5.7	—	—
IB ///	60	570	510	25°	2×10^{-18}	9×10^{-20}	4.5	34	1.2
IB ⊥⊥					1×10^{-17}	3×10^{-20}	8.3	30	1.0
CATA //⊥	64	540	480	< 30°	6×10^{-17}	9×10^{-19}	5.5	38	12.0
MB ⊥⊥	50	430	420	< 30°	2×10^{-16}	2×10^{-18}	6.0	97	3.5
DZ2 ///	94	925	560	30°	2×10^{-16}	7×10^{-18}	4.8	59	3.8

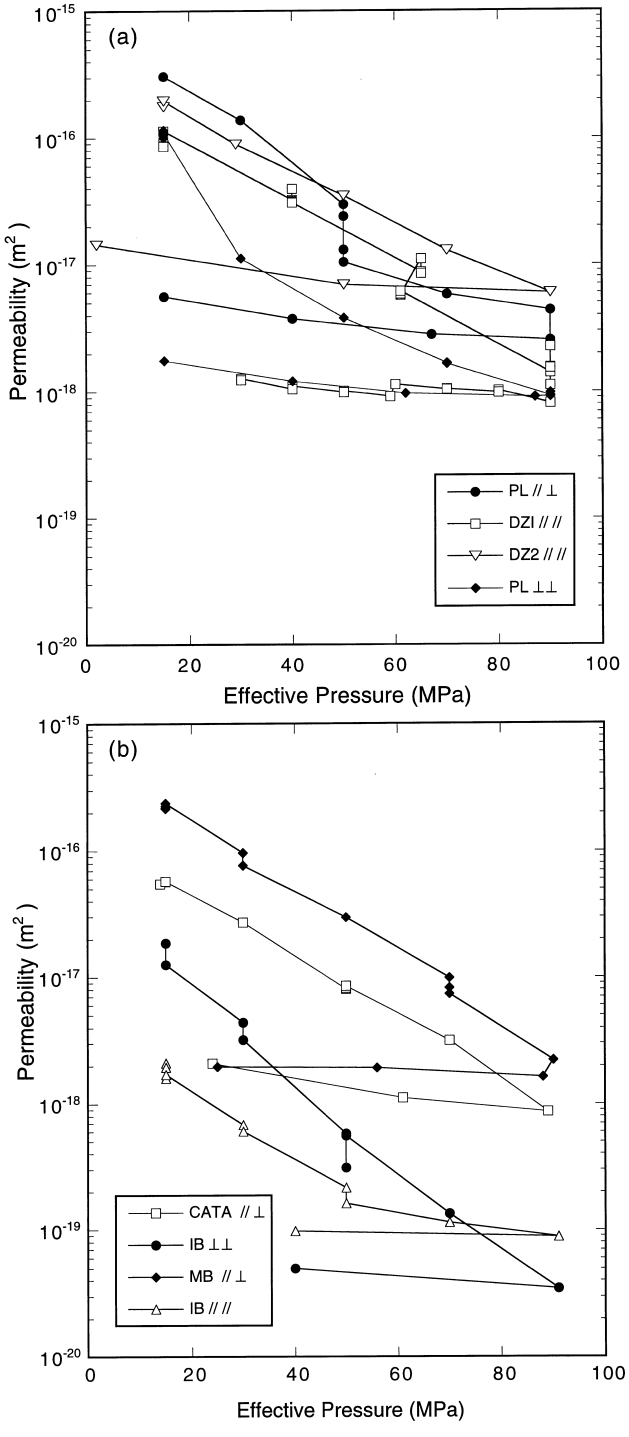

Fig. 6. Permeability data of (a) fault core, and (b) damage zone and protolith samples.

stress drops were observed in **DZ1** and post-peak deformation was catastrophic, with appreciable unstable stress drops for both samples. Failure occurred along relatively narrow conjugate faults in these samples.

PERMEABILITY AS FUNCTION OF EFFECTIVE PRESSURE

Figure 6 shows permeability as a function of effective pressure ($P_e = P_c - P_p$) for each sample tested. With the pore pressure fixed at $P_p = 10$ MPa, the confining pressure was incrementally increased to a peak value of $P_c = 100$ MPa, after which it was decreased incrementally to the initial value. Both loading and unloading segments of each test cycle are shown. Data points plotted at the same effective pressure bracket the extreme values obtained from repeatedly performing 5–20 tests for a single sample over a relatively short time interval. Some samples show a strong time-dependent decrease in permeability even when effective pressure is held constant over periods in excess of 5 h. For example, this effect was observed for **PL**//⊥ when the sample was left overnight at 50 MPa (Fig. 6).

The pressure sensitivity coefficient γ (Table 2), as defined by David *et al.* (1994), represents the way that permeability declines with increasing effective pressure. The coefficient γ is estimated using an exponential law $k = k_0\exp(-\gamma P_e)$ for P_e ranging from 15 to 90 MPa. An approximate linear relationship between log permeability and P_e is visible on the semi-logarithmic plots of Fig. 6 for all samples but **PL**⊥⊥. Values of γ range from 4.5×10^{-2} to 6.0×10^{-2} MPa^{-1} (Table 2). Although it is tempting to relate specific values of the sensitivity coefficient to each fault zone component, a clear trend is absent. Our data are comparable to values reported for crystalline rocks (David *et al.*, 1994). The coefficient γ is equivalent to the reciprocal of the parameter σ^* used by Rice (1992) to model the development of pore pressure excess in the San Andreas fault system.

The cataclasite sample (**CATA**) yields permeabilities ranging from 6×10^{-17} m^2 (at 15 MPa) to 9×10^{-19} m^2 (at 90 MPa). These values are slightly less than those of the protolith, but unexpectedly high given the relatively low porosity (< 1%) of the sample. Permeability

values obtained for damage zone sample (**DZ1**) are similar to those of the protolith samples. The permeability of the other damage zone sample (**DZ2**) is the highest observed in our sample set, 7×10^{-18} m^2 (at 90 MPa). The smallest permeabilities were found in the implosion breccia samples **IB**$/\!/\!/$ (1×10^{-17} m^2 at 15 MPa and 9×10^{-20} m^2 at 90 MPa) and **IB**$/\!/\perp$ (2×10^{-18} m^2 at 15 MPa and 3×10^{-20} m^2 at 90 MPa).

Results obtained for the two protolith samples (**PL**$/\!/\perp$ and **PL**$\perp\perp$) suggest a possible 3:1 grain scale permeability anisotropy within the protolith. The greatest resistance to fluid flow is found in a direction perpendicular to the average orientation of the fault plane (1×10^{-16} m^2 at 15 MPa and 1×10^{-18} m^2 at 90 MPa) with the least resistance to flow found parallel to the average orientation of the fault plane (3×10^{-16} m^2 at 15 MPa and 3×10^{-18} m^2 at 90 MPa).

The porosity reduction with pressure, $\Delta\phi/\Delta P$ is estimated from volumometer data (between $P_e = 15$ MPa and $P_e = 90$ MPa) and is compiled in Table 2. The data were normalized to the initial porosity of the sample providing estimates of the pore compressibility.

DISCUSSION

Mechanical strength and permeability of the fault core

To the extent that our samples are representative of the fault core, several important conclusions can be drawn from our mechanical (Fig. 5a) and hydraulic (Fig. 6a) data. First, while the fault core samples are lithified, they are weak in comparison with unaltered igneous rocks (Ohnaka, 1973) and their mechanical strengths are as low as the frictional strengths of unconsolidated gouge sandwiched in 'sawcut' samples. For the latter case, laboratory data show that frictional strength is characterized by Byerlee's (1978) law which implies that the crustal strength can be approximated by $\sigma_1 - \sigma_3 \approx 4(\sigma_3 - P_p)$ for $\sigma_3 - P_p < 110$ MPa. As elaborated on by Brace and Kohlstedt (1980), a key assumption of this strength estimate is that randomly oriented discontinuities are available so that slip can occur along surfaces with the most favorable orientation. If slip surfaces are slightly misaligned with respect to this orientation, then the frictional strength is expected to be higher. Since $\sigma_3 - P_p = 90$ MPa in our deformation experiments, the corresponding frictional strength is estimated to be ~360 MPa, comparable to the strength of 430 MPa for the weakest fault core sample (Table 2).

Second, considerable variability in permeability was observed. Core sample permeabilities at a given effective pressure differ by as much as two orders of magnitude among the fault core samples (Fig. 6a), and for a given sample the permeability may also vary by two orders of magnitude over an effective pressure range of 90 MPa. The lowest permeabilities were observed in the **IB** samples, the pore space of which had been sealed with an ultrafine-grained quartz matrix (Fig. 3b). It is of interest to note that the hydrological attributes of these lithified samples from the Stillwater fault system are in many respects similar to those of unconsolidated gouges from the San Andreas fault system (Morrow *et al.,* 1984). At elevated pressures, the permeabilities of **IB** samples and non-clay San Andreas gouge samples are of the order of 10^{-19} m^2. They all showed significant hysteresis in permeability during pressure cycles, as well as strong pressure sensitivity to changes in permeability.

The cataclasite samples (**CATA** and **MB**) have significantly higher permeabilities than the implosion breccia samples (**IB**) also obtained from the fault core. Our hydromechanical data underscore the importance of integrating laboratory and high-resolution microscopy in the study of fault rocks. From observations of hand specimens and optical microscopy alone, one could easily reach the erroneous conclusion that **CATA** (a sample that is ultrafine-grained, has very low porosity which is less than 0.5%, and an absence of microfractures resolvable by optical microscopy) should be the least permeable sample. However, our SEM observations reveal that the pore space of this sample is well connected by very thin microcracks, which probably are very effective in enhancing permeability (pore connectivity is as important as porosity in controlling the evolution of permeability).

Third, the complexity of permeability structure at all scales of observation implies that pore pressure distribution and fluid transport in the fault core are spatially and temporally heterogeneous. The fault core at the Mirrors locality is typified by pods of silicified breccia (with lengths 3–10 m and thicknesses 2–4 m) embedded in a highly silicified, ultrafine-grained cataclasite. Our experiments identify the breccia pod materials (e.g. **IB**) as the least permeable end-member at the core sample scale, with microstructures (Fig. 3b) characteristic of tectonically-driven hydrothermal implosion brecciation (Sibson, 1986a). These observations suggest that permeability of the breccia pods may undergo dramatic changes during an earthquake cycle, resulting in significant temporal variations in fluid flow. The coseismic brecciation is manifested by an instantaneous increase of permeability and massive influx of fluid (possibly expelled from storage in the damage zone). During the post-seismic period, the pore space is progressively sealed with silica (precipitating out of the fluid), with concomitant reduction of permeability and blockage of conduits. Although the fault core contains some veins, the fracture intensity is significantly lower than that of the adjacent damage zone, with minimal fault-related fracturing found in the breccia pods. While the absence of fractures in the breccia pods suggests that the laboratory data (for **IB**) represent realistic lower bounds of fault core per-

meability at the core sample scale, the field values of permeability for the cataclasite zones may be somewhat higher than our laboratory data due to mesoscopic and microscopic fracturing. Fracture enhanced permeability of the cataclasite could heighten the permeability contrasts within the fault core well above that suggested by the laboratory data. This raises the possibility that pore pressure distributions may have comparable spatial variability.

Byerlee (1993) has outlined a number of mechanical and chemical mechanisms by which compartments of anomalous pore pressure can develop in such a heterogeneous hydromechanical setting. However, hydrological analyses (Bredehoeft and Hanshaw, 1968; Walder and Nur, 1984) suggest that maintenance of such pore pressure anomalies requires permeabilities (of the order of $< 10^{-21}$ m^2), which are much lower than our laboratory measurements except for the breccia pod sample **IB**. While deformation in the low permeability breccia pods may be *locally* undrained, it is unlikely that pore pressure anomalies can be maintained *uniformly* in the fault core over the time scale of an earthquake cycle. Therefore, the average pore pressure is expected to be approximately hydrostatic and the mechanical strength approximately bounded by Byerlee's law in the interseismic period.

While these inferences on pore pressure and fault strength are consistent with Hickman and Zoback's (1997) stress measurements in a fault-hosted geothermal reservoir in Dixie Valley, they contradict the fluid inclusion data of Parry *et al.* (1991) which suggested the existence of nearly lithostatic pore pressures associated with the fault zone. One possible explanation of this apparent discrepancy is that different locations of the fault system (with different hydromechanical attributes) were sampled in these studies. Hickman and Zoback (1997) conducted their hydraulic fracturing tests in a well intersecting the Stillwater fault zone near the Mirrors locality (Fig. 1), along the seismic gap. Parry *et al.* (1991) collected their samples from the footwall of the 1954 rupture segment (Fig. 1), a locality where it was difficult for us to obtain samples of the fault core because good exposure is lacking. If this explanation applies, the implication would be that the hydromechanical properties, pore pressure distribution, and strength along this fault system are very heterogeneous. Spatial and temporal complexity in fault slip and rupture behavior are evident from geologic and seismological investigations of the 1954 Fairview and Dixie Valley earthquakes (Caskey *et al.*, 1996).

Hydromechanical properties of the damage zone and protolith

Extrapolating laboratory data from the damage zone and the protolith to the field scale and *in situ* conditions is difficult. At the core sample scale two types of complexity are incompletely represented. First, the damage zone has a dense array of mesoscopic fractures. The hydromechanical response of such a fractured medium, at the scale of a large fault zone, is such that the permeability and mechanical strength are, respectively, higher and lower than the laboratory measurements. Second, surface outcrops of the protolith show a high degree of mineralogical alteration and variable porosity which are likely to change with depth through the seismogenic crust. While a broad range of peak stresses was observed for the damage zone and protolith samples (Fig. 5b), there is a trend for strength to decrease with increasing alteration and porosity. The peak stress for the strongest sample **DZ2** falls in the high end of typical values for unaltered igneous rocks (Ohnaka, 1973). The overall strength of the protolith is expected to be higher than the fault core where inelastic deformation is localized. However, since the damage zone represents a highly fractured and veined granodiorite protolith embedded with extensional, shear and cross fractures spanning a wide range of orientations, its overall mechanical strength is governed by frictional responses of the bulk properties of potential sliding surfaces at the scale of tens to hundreds of meters. Consequently, at the field scale the damage zone is probably weaker than the laboratory samples.

Our data for permeability as a function of effective pressure (Fig. 6b) are consistent with previous studies of crystalline rocks. The pressure sensitivity of the damage zone and protolith samples are comparable to the Kola gneiss samples studied by Morrow *et al.* (1984). Because our samples are relatively porous, their permeabilities are as much as three orders of magnitude higher than low porosity rocks such as

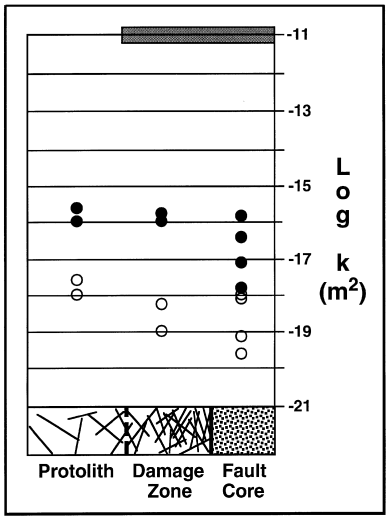

Fig. 7. Summary of laboratory permeability data obtained at $P_e = 15$ MPa (closed circles corresponding to a depth of approximately 1 km of overburden under hydrostatic pressure) and $P_e = 90$ MPa (open circles corresponding to a depth of approximately 5 km) as a function of position within the fault zone. *In situ* estimates made by Barton *et al.* (1997) at a depth of 2.5 km are shown as the shaded bar that spans the damage zone and fault core.

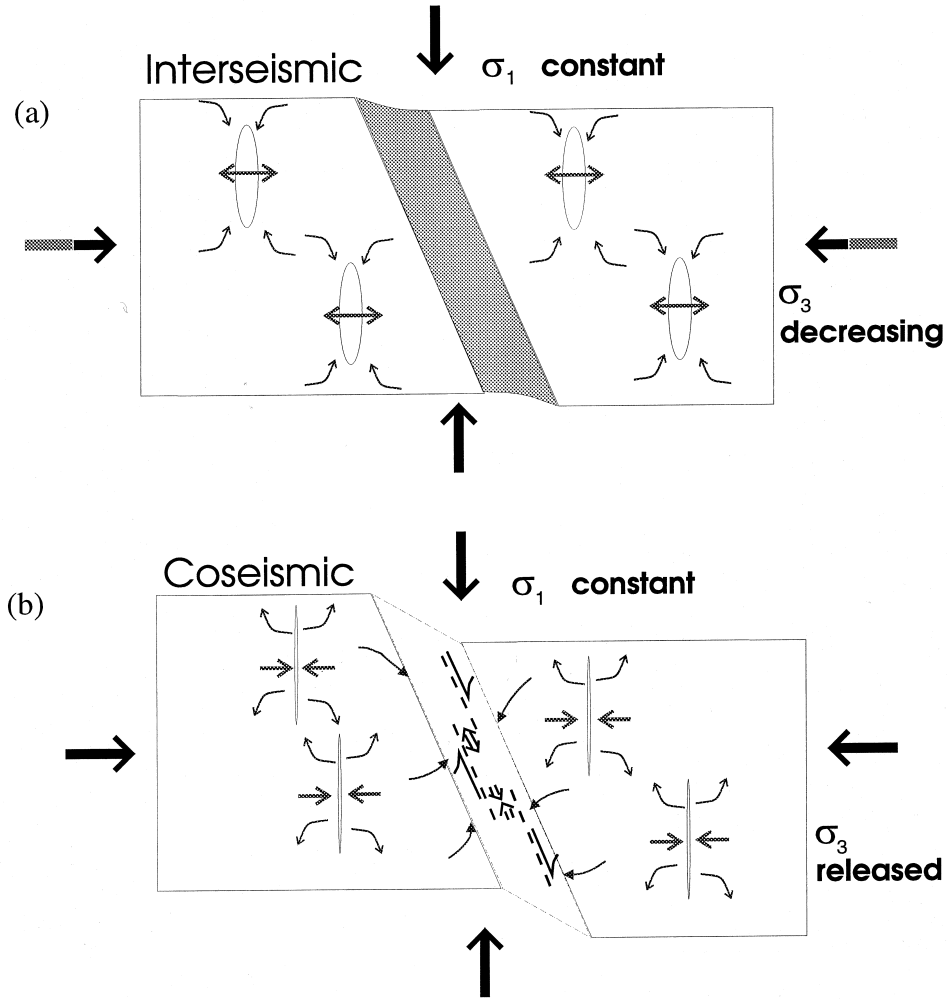

Fig. 8. Hydrological effect of extensional tectonic loading on a normal fault, after Muir Wood (1994). (a) The fault core is less dilatant and permeable than the damage zone. Fluids will be stored and flow focused in the damage zone. (b) At rupture, massive volume of fluid is released from the collapsing fractures. Permeability and porosity are enhanced in localized clusters of the fault core, to which the expelled fluid may migrate.

Westerly (Brace *et al.*, 1968) and Barre (Bernabé, 1986) granites. The high degree of alteration observed in some of our samples, may cause greater hysteresis and time-dependence than these relatively unaltered granites. Protolith samples at depth that have different alteration assemblages, may have somewhat lower permeabilities than our laboratory measurements. Because of its fractured state, the damage zone is probably more permeable than the laboratory samples (Bruhn *et al.*, 1994).

Barton *et al.* (1997) used spinner and pressure logs to identify several large-scale fluid flow anomalies within the depth interval from 2440 to 2640 m in a geothermal well located several miles northeast of the range front exposures of the Stillwater fault zone (Fig. 1). Their analysis suggests a bulk permeability of about 10^{-11} m^2 within a 2 m interval. Although these high permeabilities are clearly associated with a splay of the Stillwater fault, insufficient information is available to assess whether the high permeability zone is found within either a fault core or damage zone. In any case, the bulk permeability of the fault zone probably exceeds that of the protolith by at least five orders of magnitude (Fig. 7) and likely exceeds the permeability of breccia pods in the fault core by at least seven orders of magnitude (Fig. 7).

The large permeability contrast between fault zone and adjacent low permeability protolith suggests that fluid flow will be focused within the plane of the fault with baffles or barriers to flow across the fault being provided by the low permeability breccia pods found in the fault core. This permeability structure leads Caine *et al.* (1996) to conclude that the Stillwater fault zone represents a combined conduit-barrier flow system. Although the *in situ* test results of Barton *et al.* (1997) were obtained at relatively shallow depths (about 2.5 km), it seems reasonable to assume that the large permeability contrast between fault zone and

protolith extends to much greater depths. Given the apparent high permeability along the fault zone at the geothermal well sites it seems unlikely that elevated pore pressures would be maintained within the fault unless there is a continuous source of highly pressurized fluid (e.g. Rice, 1992). Such a mechanism requires the permeability to be sensitively dependent on the effective pressure with a coefficient $\gamma \sim 0.1$, greater than our fault rock data by one to two orders of magnitude (Table 2) but comparable to data for rock joints (David *et al.*, 1994) which presumably are analogous to fractures found in the damage zone.

Permeability structure and its evolution during the earthquake cycle

Guided by the structural framework of Caine *et al.* (1996), and Forster *et al.* (1997), we use our laboratory test results to infer the permeability structure of the Stillwater fault zone from the core sample scale to the outcrop scale (Fig. 7). As discussed above, the core sample data are probably not representative of the damage zone bulk permeability. The borehole data of Barton *et al.* (1997) is, however, included in Fig. 7 as a baseline from which to compare our data from the core scale to that of Barton's data at the scale of several meters. Unfortunately, insufficient downhole data exist to decide if the test results reported by Barton *et al.* (1997) represent the permeability of the damage zone or that of a hydrothermally altered fault core. Otherwise it is tempting to suggest that their results might be associated with the damage zone. The permeability structure shown is considered to be representative of the spatial heterogeneity in the fault system during the interseismic period. The most important conclusion of this study is that significant permeability

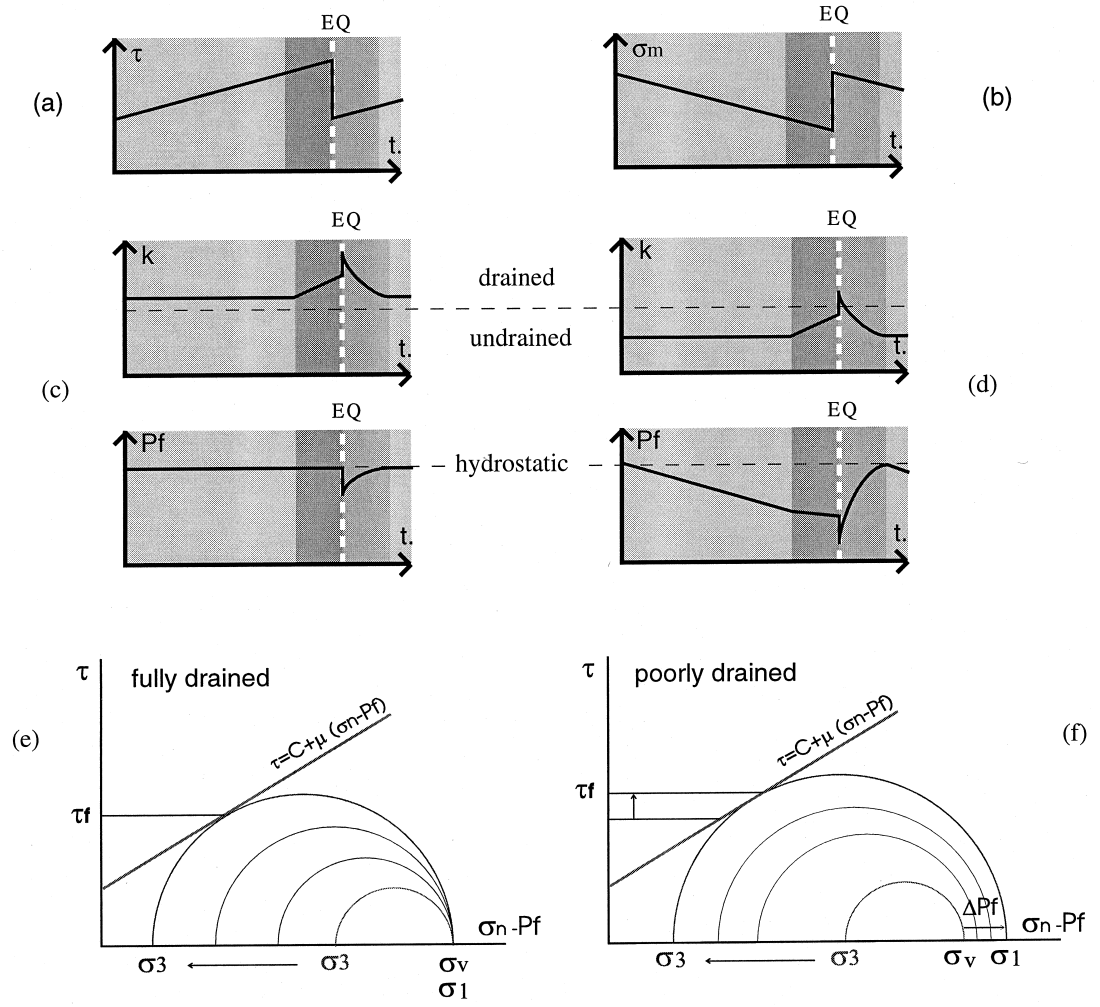

Fig. 9. Evolution of hydromechanical parameters during the seismic cycle. The time of dynamic rupture in the coseismic stage is indicated by the white dashed line marked 'EQ', and the pre-seismic, post-seismic, and interseismic stages are shown in decreasing grey levels. (a) Remote shear stress on the fault plane. (b) Remote mean stress on the fault plane. (c) Evolution of permeability and corresponding pore pressure in the drained part (cataclasite) of the fault core. (d) Evolution of the permeability and corresponding pore pressure in the poorly drained part (breccia pods) of the fault core. (e) Mohr representation of the loading to rupture in drained conditions. (f) Corresponding loading of a poorly drained cluster undergoing dilatancy hardening.

contrasts occur at two very different spatial scales. At the core sample scale the breccia pods represent clusters of low permeability embedded in relatively more permeable cataclasites. In addition the breccia pods have a permeability about one order of magnitude less than the protolith samples. At the fault scale *in situ* tests suggest that the permeability of the damage zone–core composite is at least five orders of magnitude greater than that of the protolith.

During an earthquake cycle, the permeability structure is expected to evolve with the evolving tectonic stress field (e.g. Sibson, 1986b). The scenarios are schematically illustrated in Figs 8 and 9. The earthquake cycle is often divided into four stages: pre-seismic, coseismic, post-seismic, and interseismic (Scholz, 1990). In the coseismic stage, dynamic deformation occurs almost instantaneously with the earthquake rupture. Nonlinear accumulation of deformation with time is observed for some time before and after the rupture, corresponding to the pre-seismic and post-seismic phases respectively. By far the longest duration is taken up by the interseismic stage, during which the loading is approximately linear.

In a normal fault system, the maximum principal stress (σ_1) is vertical whereas the intermediate and minimum principal stresses (σ_2 and σ_3) are horizontal. The vertical stress due to the overburden remains relatively constant throughout the earthquake cycle. During the interseismic stage, the horizontal stresses steadily decrease in response to extensional tectonic loading (Figs 8a & 9a). Deformation in the fault system is primarily poroelastic, and since the mean stress steadily decreases (Fig. 9b), the pore space undergoes elastic dilation. Dilation is most pronounced in the most elastically compliant member of the fault system, namely the fracture arrays in the damage zone. Given the relatively high permeability of the damage zone (Fig. 7), fluids will readily percolate from the surrounding region into the damage zone for storage in the dilating fractures (Muir Wood, 1994).

During the interseismic stage, the shear stress increases (Fig. 9a) and the evolution of the stress field is characterized by a Mohr circle which expands with the extensional loading (Fig. 9e) steadily approaching the failure envelope. When loaded beyond the critical stress C' (Fig. 6a & b) our laboratory samples showed appreciable inelastic dilatancy, which contributes to non-linear deformation in the pre-seismic stage. Shear-enhanced dilation of the pore space increases overall fluid storage in the seismogenic system. Furthermore, it may result in anomalous pore pressure distribution in the system where there is a high permeability contrast. Localized clusters of low permeability may be hydraulically isolated so that their deformation evolves under 'undrained' conditions. If dilatancy occurs in the breccia pods of the fault core and if the permeability is sufficiently low that the pore volume increase cannot be rapidly filled by the influx of fluid, then localized domains of pore pressure *deficit* would develop throughout the fault core during the preseismic stage. Due to dilatancy, the pore pressures within the breccia pods may be anomalously low and consequently the effective pressures anomalously high, thus delaying the occurrence of failure. The Mohr circle corresponding to this phenomenon of '*dilatancy hardening*' (Brace and Martin, 1968; Rudnicki and Chen, 1988) is illustrated in Fig. 9(f).

Our laboratory data provide quantitative constraints on the charcteristic time scale t_c during which undrained deformation and dilatancy hardening may occur in localized clusters in the fault core during the preseismic stage. Hydraulic diffusion into the breccia pods is governed by the diffusivity (D):

$$D = \frac{k}{\mu\phi(\beta_\phi + \beta_f)}$$

where k is permeability, μ is viscosity, ϕ is porosity, β_ϕ is pore compressibility, and β_f is fluid compressibility (Brace and Martin, 1968; Walder and Nur, 1984). From our laboratory measurements for sample **IB**, $k \sim 5 \times 10^{-20}$ m^2, $\phi \sim 3\%$ and $\beta_\phi \sim 10^{-9}$ Pa^{-1}, and assuming typical values of $\mu = 10^{-3}$ Pa s and $\beta_f = 5 \times 10^{-10}$ Pa^{-1} for water, we estimate the hydraulic diffusivity to be $D \sim 1.1 \times 10^{-6}$ m^2 s^{-1}. From field observations, a representative dimension of a large breccia pod is $L \sim 10$ m. Thus, the characteristic time required for the dissipation of pore pressure anomaly is $t_c \sim L^2/D = 2.9$ years. It should be noted that the above choices of physical and geometric parameters are subject to several sources of uncertainty. The permeability may increase somewhat with the development of dilatancy (Zoback and Byerlee, 1975). The viscosity and compressibility of water may increase (decrease) with increasing pore pressure (temperature). Nevertheless, the above should be considered a realistic order-of-magnitude estimate of the time scale over which partially undrained deformation and dilatancy hardening can occur in isolated clusters of the fault core.

If the deformation is completely undrained, then the laboratory data can also be used to place an upper bound on the pore pressure change, which is given by $\Delta P_p \sim -(\Delta\phi/\phi)/\beta_f$ for a porosity change $\Delta\phi$. When loaded from C' to peak stress, the porosity of sample **IB** increased by as much as 0.1% (Fig. 5a), which would result in a pore pressure deficit as high as $\Delta P_p = -67$ MPa. This upper bound can be attained only if the material is completely impermeable.

If indeed the dilatancy hardening effect is effective in delaying failure and 'locking up' the breccia pods, then their failure and brecciation processes are analogous to what has been postulated by Sibson (1986a) for dilatational fault jogs, with an important difference that

fault jogs are usually attributed to geometric irregularities whereas the pods here are 'locked up' due to their permeability heterogeneity and the resulting undrained deformation. As elaborated by Sibson (1986b), the fault jogs act as local barriers to the coseismic development of slip discontinuity within the fault core (Fig. 8b). Subsequent failure of these dilatational jogs would result in permeability enhancement, which provides conduits for fluid to fill in the voids during the postseismic stage. The evolution of permeability and pore pressure in the breccia pods follow somewhat different paths from the rest of the fault system (Fig. 9c). Over several earthquake cycles, the fault jogs would be subjected to multiple episodes of implosion brecciation and hydrothermal cementation, producing microstructures analogous to those of the **IB** samples (Table 1 & Fig. 3c).

CONCLUSION

Our study provides useful hydromechanical constraints on the permeability structure, pore pressure distribution and mechanics of faulting along the Stillwater fault zone. Specifically we arrive at the following conclusions on the basis of results presented herein.

1. Dilatancy and conjugate faulting were observed in all of our samples. Possibly due to the low cohesion of the cemented bonds and composition, the fault core samples were relatively weak, with peak stresses approaching those of unconsolidated fault gouges. In comparison, the granodiorite samples from the protolith had similar strengths to that of the fault core samples and the damage zone samples were stronger than samples from the fault core. Protolith and damage zone samples showed peak stresses increasing with decreasing porosity and degree of alteration.

2. Permeability decreased with increasing effective pressure, decreasing porosity and connectivity of pore space. Our measurements range over four orders of magnitude, from 10^{-20} m^2 to 10^{-16} m^2. The lowest permeability of 3×10^{-20} m^2 was measured in a fault core sample with microstructures indicative of implosion brecciation. Magnitude and pressure sensitivity of permeability in our cemented fault core samples are comparable to those observed in unconsolidated fault gouge samples from the San Andreas fault system.

3. In conjunction with other field measurements, the laboratory data suggest that hydraulic flow and storage are concentrated in the fractures of the damage zone, with permeability several orders of magnitude higher than the protolith and fault core. It is unlikely that pore pressure excess can be maintained in the highly permeable damage zone, unless there is massive influx of fluids.

4. At the core sample scale, significant permeability contrast exists between the cataclasite and breccia in the fault core. With the onset of dilatancy in the preseismic stage, anomalously low pore pressures may develop in the poorly drained breccia pods. These clusters of low pore pressure can potentially act as fault jogs, locally locking up the fault due to dilatancy hardening. Delayed failure may finally occur in these fault jogs in the post-seismic stage, with catastrophic implosion rupture and brecciation.

Acknowledgements—We are grateful to Dick Yund for the use of his ion milling facilities at Brown University, and Alice Post for her help. We have benefited from several useful discussions with Steve Hickman. The collaborative research (originally proposed between the University of Utah and TerraTek Inc.) was supported by the U.S. Geological Survey NEHRP program through a grant to C. B. Forster, R. L. Bruhn and J. T. Fredrich (Grant No.1434-93-G2280). The laboratory study at Stony Brook was also supported by the National Science Foundation under grant EAR9508044. Portions of this work were performed at Sandia National Laboratories supported by the U.S. Department of Energy under Contract No. DE-AC04-AL85000.

REFERENCES

Barton, C. A., Hickman, S., Morin, R., Zoback, M. D., Finkbeiner, T., Sass, J. and Benoit, D. (1997) Fracture permeability and its relationship to *in-situ* stress in the Dixie Valley, Nevada, geothermal reservoir. *Proceedings of the 22nd Workshop on Geothermal Reservoir Engineering*. Stanford University, Stanford, California.

Bernabé, Y. (1986) The effective pressure law for permeability in Chelmsford granite and Barre granite. *International Journal of Rock Mechanics, Mineral Science and Geomechanical Abstracts* **23,** 267–275.

Brace, W. F. and Kohlstedt, D. L. (1980) Limits on lithospheric stress imposed by laboratory experiments. *Journal of Geophysical Research* **85,** 6248–6252.

Brace, W. F. and Martin, R. G. I. (1968) A test of the law of effective stress for crystalline rocks of low porosity. *International Journal of Rock Mechanics and Mineral Science* **5,** 415–426.

Brace, W. F., Walsh, J. B. and Frangos, W. T. (1968) Permeability of granite under high pressure. *Journal of Geophysical Research* **73,** 2225–2236.

Bredehoeft, J. D. and Hanshaw, B. B. (1968) On the maintenance of anomalous fluid pressures, I. Thick sedimentary sequences. *Geological Society of America Bulletin* **79,** 1097–1106.

Bruhn, R., Parry, W., Yonkee, A. and Thompson, T. (1994) Fracturing and hydrothermal alteration in normal fault zones. *Pure and Applied Geophysics* **142**(3/4), 609–644.

Byerlee, J. D. (1978) Friction of rocks. *Pure and Applied Geophysics* **116,** 615–626.

Byerlee, J. D. (1993) A model for episodic flow of high pressure water in fault zones before earthquakes. *Geology* **21,** 303–306.

Caine, J. S., Evans, J. P. and Forster, C. B. (1996) Fault zone architecture and permeability structure. *Geology* **24,** 1025–1028.

Caskey, S. J., Wesnousky, S. G., Zhang, P. and Slemmons, D. B. (1996) Surface faulting of the 1954 Fairview Peak (M_S 7.2) and Dixie Valley (M_S 6.8) earthquakes, central Nevada. *Bulletin of Seismological Society of America* **86,** 761–787.

David, C., Wong, T-f, Zhu, W. and Zhang, J. (1994) Laboratory measurement of compaction-induced permeability change in porous rock: implications for the generation and maintenance of pore pressure excess in the crust. *Pure and Applied Geophysics* **143,** 425–456.

Dozer, D. I. (1986) Earthquake processes in the Rainbow mountain–Fairview Peak–Dixie valley, Nevada, region 1954–1959. *Journal of Geophysical Research* **91,** 12,572–12,586.

Forster, C. B., Caine, J. S., Schulz, S. and Nielson, D. L. (1997) Fault zone architecture and fluid flow: An example from Dixie

Valley, Nevada. *Proceedings of the 22nd Workshop on Geothermal Reservoir Engineering*. Stanford University, Stanford, California.

Hickman, S., Sibson, R. and Bruhn, R. L. (1995) Introduction to special section: Mechanical involvement of fluids in faulting. *Journal of Geophysical Research* **100,** 12,831–12,840.

Hickman, S. and Zoback, M. (1997) *In-situ* stress in a fault-hosted geothermal reservoir at Dixie Valley, Nevada. *Proceedings of the 22nd Workshop on Geothermal Reservoir Engineering*. Stanford University, Stanford, California.

Hsieh, P. A., Tracy, J. V., Neuzil, C. E., Bredehoeft, J. D. and Silliman, S. E. (1981) A transient laboratory method for determining the hydraulic properties of 'tight' rocks—I. Theory. *International Journal of Rock Mechanics, Mineral Science and Geomechanical Abstracts* **18,** 245–252.

Morrow, C. A., Shi, L. Q. and Byerlee, J. D. (1984) Permeability of fault gouge under confining pressure and shear stress. *Journal of Geophysical Research* **89,** 3193–3200.

Wood Muir, R. (1994) Earthquakes, strain cycling and the mobilization of fluids. In *Geofluids, Origin, Migration and Evolution of Fluids in Sedimentary Basins*, ed. J. Parnell, pp. 85–98. Geological Society Special Publications **78**.

Ohnaka, M. (1973) The quantitative effect of hydrostatic confining pressure on the compressive strength of crystalline rocks. *Journal of Physics of the Earth* **21,** 125–140.

Page, B. M. (1965) *Preliminary Geologic Map of a Part of the Stillwater Range, Churchill County, Nevada.* Nevada bureau of mines and geology, Reno, Nevada, U.S.A.

Parry, W. T., Hedderly-Smith, D. and Bruhn, R. L. (1991) Fluid inclusions and hydrothermal alteration on the Dixie valley fault, Nevada. *Journal of Geophysical Research* **96,** 19733–19748.

Power, W. L. and Tullis, T. E. (1989) The relation between slickenside surfaces in fine-grained quartz and the seismic cycle. *Journal of Structural Geology* **11,** 879–893.

Rice, J. R. (1992) Fault stress states, pore pressure distributions, and the weakness of the San Andreas fault. In *Fault Mechanics and Transport Properties of Rocks*, eds B. Evans and T.-F. Wong, pp. 475–504. Academic Press, San Diego.

Rudnicki, J. W. and Chen, C. J. (1988) Stabilization of rapid frictional slip on a weakening fault by dilatant hardening. *Journal of Geophysical Research* **93,** 4745–4757.

Scholz, C. H. (1990) *The Mechanics of Earthquakes and Faulting*. Cambridge University Press, Cambridge.

Sibson, R. H. (1986a) Brecciation processes in fault zones: inferences from earthquake rupturing. *Pure and Applied Geophysics* **124,** 159–176.

Sibson, R. H. (1986b) Earthquakes and rock deformation in crustal fault zones. *Annual Reviews in Earth and Planetary Sciences* **14,** 149–175.

Sibson, R. H. (1994) Crustal stress, faulting and fluid flow. In *Geofluids, Origin, Migration and Evolution of Fluids in Sedimentary Basins*, ed. J. Parnell, pp. 69–84. Geological Society Special Publications **78**.

Trimmer, D. A. (1981) Design criteria for laboratory measurements of low permeability rocks. *Geophysical Research Letters* **8,** 973–975.

Walder, J. and Nur, A. (1984) Porosity reduction and crustal pore pressure development. *Journal of Geophysical Research* **89,** 11539–11548.

Wallace, R. E. and Whitney, R. A. (1984) Late quaternary history of the Stillwater seismic gap, Nevada. *Bulletin of the Seismological Society of America* **74,** 301–314.

Zoback, M. D. and Byerlee, J. D. (1975) The effect of cyclic differential stress on dilatancy in Westerly granite under uniaxial and triaxial conditions. *Journal of Geophysical Research* **80,** 1526–1530.